Advances in Science and Technology Research Journal

Advances in Science and Technology Research Journal 2024, 18(5), 217–233
https://doi.org/10.12913/22998624/191014
ISSN 2299-8624, License CC-BY 4.0

Received: 2024.05.09
Accepted: 2024.07.20
Published: 2024.08.01

Laser Ultrasonic Technique for Simultaneous Measurement of Thickness, Slope, and Wave Velocities for Slope Plate in the Thermoelastic Regime

Nguyen Tien Dung[1,2], Yoshio Arai[1*]

[1] Division of Mechanical Engineering and Science, Saitama University, 255, Shimo-ookubo, Sakura-ku, Saitama, 338-8570 Japan

[2] Faculty of Mechanical Engineering, Hanoi University of Civil Engineering, 55, Giai Phong Road, Hai Ba Trung District, Hanoi, 100000 Vietnam

* Corresponding author's e-mail: yarai@mail.saitama-u.ac.jp

ABSTRACT

This study introduces a reliable method for simultaneously determining the thickness, slope, and ultrasonic velocities of slope plates using laser ultrasonic techniques without any damage in the thermoelastic regime. The method involves solving a system of Equations to determine the arrival times of multiple signals displayed on a waveform. Numerical simulations indicate that the velocity of the skimming longitudinal wave remains constant when the Rayleigh wave does not overlap with its signal. Consequently, a prediction model for aluminum alloy has been established, enabling the estimation of the constant ratio between the velocities of skimming longitudinal and bulk longitudinal waves based on the skimming longitudinal velocity obtained by scanning the generating laser along the material's surface. This ratio, approximately 0.950, facilitates the combination of the skimming longitudinal wave with the reflected and mode-converted waves from the specimen's back surface to deduce the desired parameters. The method successfully determined the thickness, slope, and wave velocities of several specimens with slopes ranging from 0% to 1.96% and a maximum thickness of about 10 mm. Evaluating the influence of the size of the disk ultrasound source produced by the unfocused laser beam, we found that the radius of the disk source should be considered when calculating the arrival time of the skimming longitudinal wave. The root mean square deviation in measuring thickness, slope, longitudinal wave velocity, and shear wave velocity were approximately 0.100 mm, 0.10%, 70 m/s, and 20 m/s, respectively. An assessment of the measured results, based on the root mean square deviation and uncertainty across all specimens, demonstrates the practical feasibility of the proposed method.

Keywords: laser ultrasonic, thickness, slope; skimming longitudinal wave, multiple wave mode, simultaneous measurement.

INTRODUCTION

Steel beams with C-shaped or I-shaped cross-sections are extensively utilized in various industries for metal structures. The flange thickness of these beams changes because it is designed to optimize the distribution of load and structural stability while minimizing material usage. The flange thickness directly impacts the load-bearing capacity and stability of the steel beam, making thickness measurement play an important role in structural assessments, maintenance, and quality control. However, this flange section features a one-side slope surface located on the inner side of the beam, posing numerous challenges for contact measurements. Recently, laser ultrasound methods have garnered significant attention for product quality management in industries, owing to their non-contact nature and rapidity [1–3]. In the laser ultrasound technique, a pulsed laser is utilized to excite the surface of the object inducing ultrasonic waves, while another laser is employed to detect the surface motion produced by these waves. For non-destructive ultrasonic

testing, techniques that utilize laser-generated ultrasonic waves in the thermoelastic regime are being developed to replace the ablation regime, which causes surface damage [2]. Therefore, the laser ultrasonic is expected to be applicable to monitor the thickness of metal structures that have a cross-section with variable thickness.

The normal pulse-echo method in the reflection configuration is a popular ultrasonic technique for estimating the thickness from access to one side of the object. This method relies on measuring the flight time of ultrasonic waves corresponding to the propagation wave path and their propagation velocity to calculate the thickness. The laser ultrasonic technique, utilizing the pulse-echo technique, has been successfully applied for inspecting thickness measurement of seamless tubes and rolled steels in production lines [4, 5]. The maximum thickness measurable under laboratory conditions is reported to be 100 mm [6] using the ablation regime. Research by Kruger [6] and Li [7] also shows that the technique is applicable at elevated temperatures. Rahim [8] successfully utilized this method to inspect thickness variations induced by the spinning process on an aluminum tube, accurately measuring the hill and valley features of the rough surface. However, the precision of thickness measurement in these studies heavily relies on accurately determining the velocity of ultrasound waves beforehand. In addition, due to the directivity pattern characteristics of laser-generated ultrasonic waves, the normal pulse-echo method is solely applicable in the ablation regime when the longitudinal wave achieves its maximum amplitude with a propagation angle perpendicular to the surface [9–11]. Conversely, in the thermoelastic regime, the orientation angles of the shear wave and longitudinal wave are 30 degrees and 60 degrees, respectively, rendering this technique unsuitable [12].

By separating the generating and receiving laser, multiple wave modes can be obtained due to the broadband properties of the receiving laser providing various important information about the material. That allows multiple material parameters to be determined simultaneously in one measurement. Falkenström and Engman [13] outlined a technique for gauging the thickness and longitudinal wave velocity of 4 and 5 – mm thick specimens by analyzing successive longitudinal echoes on a waveform, employing separate generating, and receiving lasers under the ablation regime. Chen [14] overcame the low signal-to-noise ratio of ultrasonic signals due to the rough surface of ductile iron pipe to determine the thickness and longitudinal wave velocity. The scanning of the receiving laser is carried out in the oblique transmission configuration to simultaneously calculate longitudinal wave velocity and thickness. Several studies have conducted measurements of thickness, longitudinal wave velocity, and shear wave velocity, employing fitting techniques for Lamb wave dispersion curves propagated in thin materials [15, 16]. In our previous study [17], we successfully employed a combination of laser-generated multiple wave modes in the thermoelastic regime to simultaneously determine the thickness and velocity of longitudinal and shear waves. By predetermining the ratio between the velocity of the skimming longitudinal waves and bulk longitudinal wave on the reference specimen, we have solved the system of Equations for the arrival time of the multiple signals appearing on a waveform based on their propagation wave paths applied in the plate plane. The limitation of this study is that it must use reference specimens, leading to errors in the calculation process. In addition, this study [17] is also subject to the same limitation as previous studies [13–16] in that the technique is only applicable to a plane plate. The influence of reflective slope surfaces on calculation has not been mentioned in these studies.

In this study, we propose a reliable method to simultaneously determine the thickness, slope, and ultrasonic wave velocity of a one-side slope plate made from aluminum alloy 6061 (AA6061). A specific study was conducted based on numerical simulation for a plane-structure model, allowing the determination of the properties of skimming longitudinal wave velocity propagated along the surface, depending on the distance between two laser beams. In addition, a proposed model was established to predict the velocity ratio of skimming longitudinal waves to bulk longitudinal waves. This model enables the determination of the ratio based on the velocity of the skimming longitudinal wave obtained by scanning the generating laser along the surface of the slope specimen. To obtain the desired information, the system of Equations for calculating the arrival times of multiple signals, including guided waves and bulk waves, expressed on a waveform and considering the slope of the back surface, is solved. To assess the proposed method, five specimens with slopes ranging from 0% to 2% were used for ultrasonic testing. This study also evaluated the

influence of the ultrasonic source size, generated by the Gaussian laser, on the results.

THEORY AND NUMERICAL SIMULATION

Laser-generated ultrasound in the thermoelastic regime

The high-energy pulsed laser beam irradiates the surface of the material, causing partial absorption of the energy and subsequent rapid local heating. This increase in temperature leads to the thermal expansion of the material and the generation of stress waves due to sudden volume changes. These stress waves propagate away from the laser-irradiated spot as ultrasonic waves. This process is theoretically described based on the utilization of heat conduction and thermoelastic displacement Equations [18, 19]. These Equations can be expressed in a cylindrical coordinate system as follows:

$$\rho c(T)\frac{\partial T(r,z,t)}{\partial t} = \frac{1}{r}\frac{\partial}{\partial t}\left(rk(T)\frac{\partial T(r,z,t)}{\partial r}\right) + \\ + \frac{\partial}{\partial z}\left(k(T)\frac{\partial T(r,z,t)}{\partial z}\right) \quad (1)$$

where: $T(r,z,t)$ – temperature distribution at time t, r – radial direction, z – cylindrical axis, ρ – density, $c(T)$ – temperature-dependent specific heat capacity, $k(T)$ – temperature-dependent thermal conductivity.

The displacement coupled with thermal expansion for isotropic material can be expressed as follows:

$$(\lambda+\mu)\nabla\big(\nabla\cdot U(r,z,t)\big) + \mu\nabla^2 U(r,z,t) - \\ - \alpha(T)(3\lambda+2\mu)\nabla T(r,z,t) = \rho\frac{\partial^2 U(r,z,t)}{\partial^2 t} \quad (2)$$

where: $U(r,z,t)$ – time-dependent displacement, $\alpha(T)$ – temperature-dependent thermal expansion coefficient, λ (Lamé's first parameter) and μ (Lamé's second parameter) – Lamé constants.

Because the laser spot on the surface of the material is a Gaussian beam considered as a disk source, an axisymmetric model is established. Fig. 1a depicts this model, where H and W represent the thickness and half-width of the model, respectively. The stress-free boundary condition is met on the surface of the model. In the thermoelastic regime, the laser heat source is commonly treated with heat flux at the excited surface. Therefore, the boundary conditions of the laser-excited surface concerning surface radiation are described by the following Equation:

$$-k(T)\left.\frac{\partial T(r,z,t)}{\partial z}\right|_{z=0} = AI_0 f(r)g(t) \quad (3)$$

where: I_0 – incident laser power density, A – optical absorption, $f(r)$ – spatial distribution of laser, $g(t)$ – temporal distributions of laser. In this case, these two functions can be written as:

$$f(r) = e^{\left(-\frac{r^2}{r_0^2}\right)} \quad (4)$$

$$g(t) = \left(\frac{t}{t_0}\right)^4 e^{4\left(1-\frac{t}{t_0}\right)} \quad (5)$$

where: r_0 – radius of the laser beam when the intensity drops to $1/e$ of its maximum intensity, t_0 – arrival time of peak value.

The boundary condition applied for the back surface and side surface is:

$$k(T)\left.\frac{\partial T(r,z,t)}{\partial z}\right|_{z=H} = k(T)\left.\frac{\partial T(r,z,t)}{\partial z}\right|_{r=W} = 0 \quad (6)$$

The initial condition of the temperature field is:

$$T(r,z,t)|_{t=0} = 300\ K \quad (7)$$

In the numerical model, the temperature-dependent material properties of AA 6061 [20] were utilized. An axisymmetric model with dimensions of H = 10 mm and W = 24 mm was established. Laser properties, including the temporal distribution and spatial distribution, were determined by the experiment. Figure 1b describes the temporal distribution for the laser measured by the photodetector. The fitting curve to Equation 5 of the experimental data was used as the amplitude of the surface heat flux in the simulation. In Fig. 1c, the spatial distribution of the laser spot was measured using the technique described by Magnes [21]. The Gaussian profile of the surface heat flux according to Equation 4 with a radius r_0 = 0.9 mm was employed in the simulation. The front surface of the model was fully illuminated by the laser, producing a surface heat flux magnitude set at 6×10^{11} W/m^2. The optical absorption of the laser by aluminum at a wavelength of 1064 nm was determined to be 0.06 [2]. The propagation of ultrasonic waves induced by the pulsed laser was simulated using the commercial

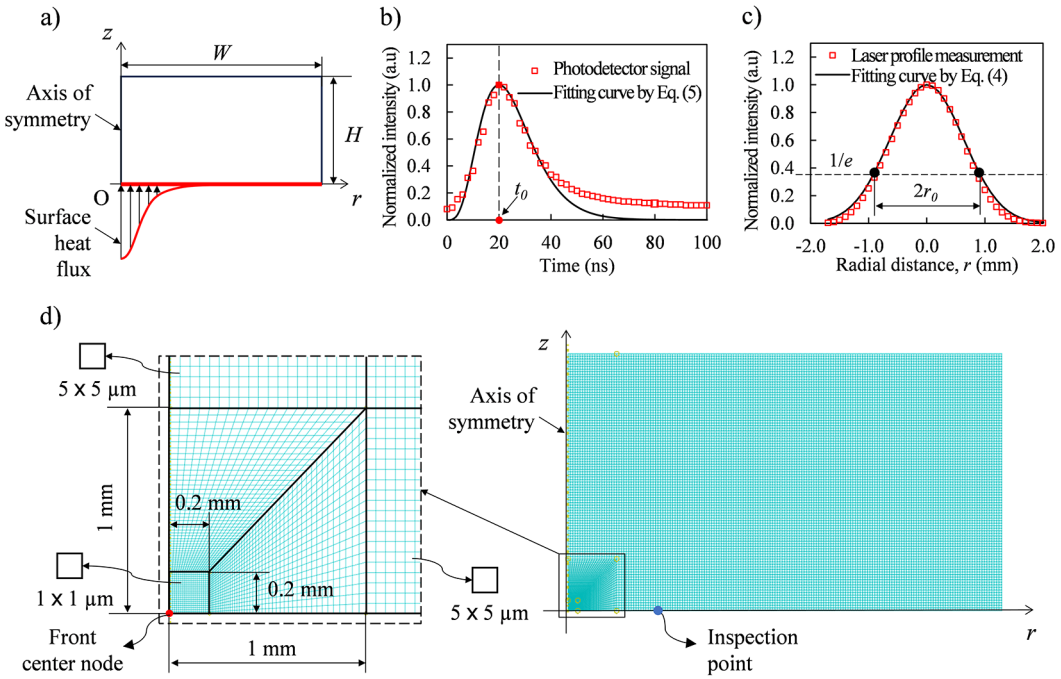

Figure 1. (a) Numerical model to simulate the laser-generated ultrasonic wave in the thermoelastic regime, (b) laser temporal distribution, (c) laser spatial distribution, (d) mesh design

ABAQUS software, employing the explicit module of dynamic, temperature-displacement analysis. A mesh convergence study was conducted to assess the mesh size based on the criteria of temperature of the front center node and the velocities of longitudinal wave and skimming longitudinal wave. In Figure 1d, a proper mesh design with a minimum element size of 1 µm gradually increases to a maximum element size of 5 µm was applied to an area measuring 1×1 mm, corresponding to the laser spot radius of around 1 mm, while a mesh size of 5 µm was utilized for the remaining section of the model.

Simulated results

Figure 2 presents a contour plot depicting the magnitude of the displacement velocity extracted from simulated results at sequential times, illustrating the propagation of ultrasonic waves. The bulk longitudinal and shear waves are denoted as *P* and *S* waves, respectively. The guided wave, inclusive of the Rayleigh wave and skimming longitudinal wave, is denoted as *R* and *sP*, respectively. At 0.2 µs, as the *P* wave begins to separate from the other waves, the *S* wave blends with the guided waves in the local region irradiated by the laser, making it difficult to distinguish them. As time progresses, distinct wave modes become apparent due to their different velocities. Indeed, at 1.1 µs, clear contours of bulk waves (*P* and *S* waves) and guide waves (*sP* and *R* waves) are observed. Upon reaching the back surface, *P* and *S* waves produce both reflected and mode-converted waves. Specifically, the presence of the first reflected longitudinal wave (*2P*) and mode-converted shear wave (*1P1S*) is observed at 2 µs. Similarly, at 3.7 µs, the *S* wave reflects as the first reflected shear wave (*2S*) and mode-converted longitudinal wave (*1S1P*). By 4.7 µs, as *1S1P* and *1P1S* approach the front surface, the intensity of *1S1P* notably surpasses that of *1P1S*. Hence, the displacement velocity of the node on the surface resulting from the mode-converted wave is predominantly contributed by the *1S1P*. The *2S* is the last reflected wave backs to the front surface during the observed period.

Figure 2b and Figure 2c depict the wavefronts of the *P* and *S*, respectively. The wavefronts are characterized by a quarter-circle shape representing a spherical wavefront, along with a section extending parallel to the front surface denoting the flat wavefront. The simulated results are consistent with the Huygens principle, which considers the ultrasound source to be a plane disk source formed by a combination of point sources with the boundary gathered by the centre of the spherical wavefront. Every point in the source can be

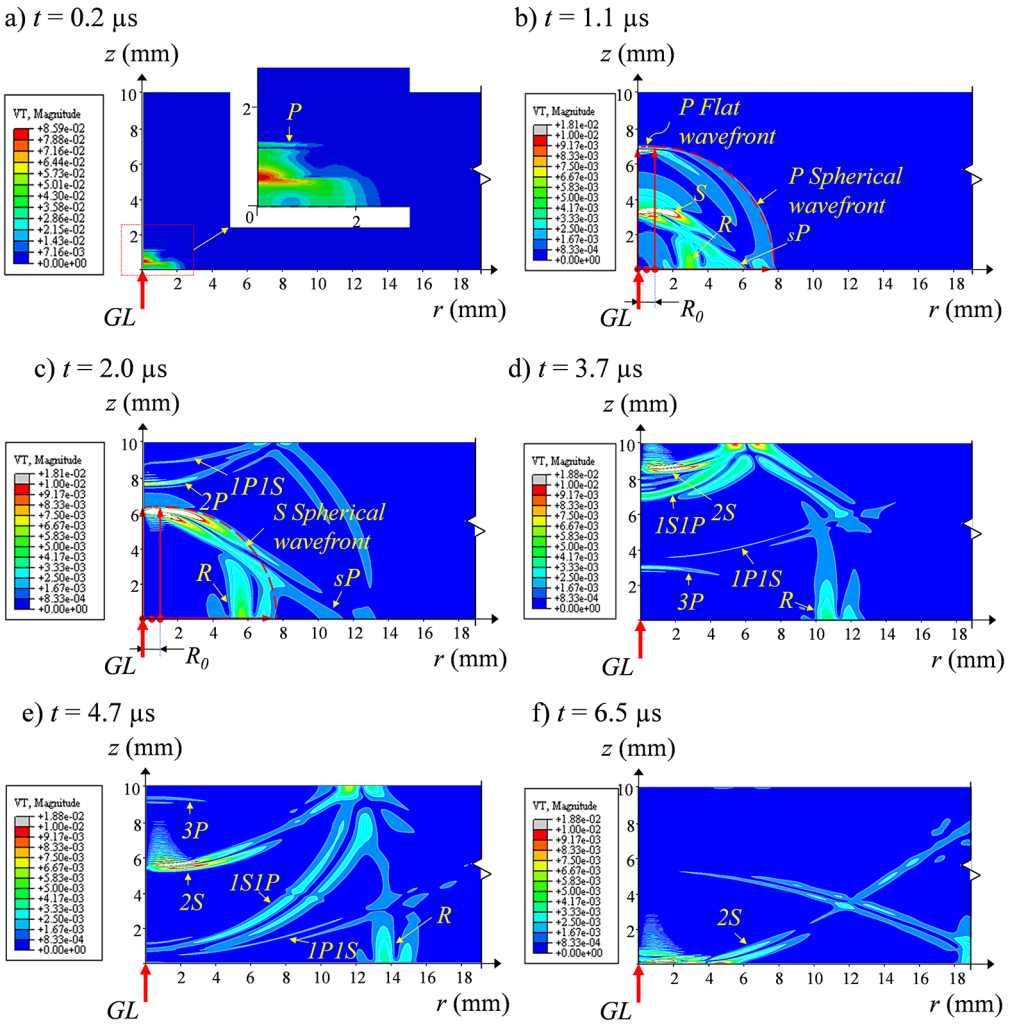

Figure 2. Wave propagation in the thermoelastic regime

considered as a point source that produces spherical waves in an ideal isotropic medium. The interference of multiple wavefronts originating from the points on the plane disk source generates the propagation of the wavefronts with the shape illustrated in Figure 2b and Figure 2c. Considering the concept of ray tracing in the application of ultrasonic technique, the incident and reflected waves can be treated as multiple individual ray paths originating from the point source. Therefore, the displacement velocity of the node on the surface caused by each wave mode in the time domain is considered an interference of the signals generated by these point sources. Achenbach [22] theoretically explained the propagation of surface waves at the thermoelastic regime by considering the ultrasonic source as a plane disk source. However, the appearance and propagation of *sP* wave with velocity close to *P* wave has not been mentioned in this study.

Figure 3a presents the time-position images showing the normalized intensity of displacement velocity normal to the surface, derived from several points located along the front surface from the simulation, with the increment space of 0.1 mm. When changing the radial distance, the signals of *sP*, *R*, *2P*, *1S1P* and *2S* are shown by continuous curves. It is clearly shown that the arrival time of *sP* has a linear relationship with the radial distance. In the simulation, the laser irradiates the entire surface, with intensity decreasing as the radial distance increases. However, in Fig. 3a, the intersection point of the *sP* curve with the vertical axis is non-zero, suggesting that the *sP* signal emerges suddenly at a location other than the center of the source on the surface. This behavior aligns with that of a disk source, as discussed above. The edge of the ultrasonic disk source, with a radius of R_0, acts as the starting point of the *sP* wave. Figure 3b shows that the signals of

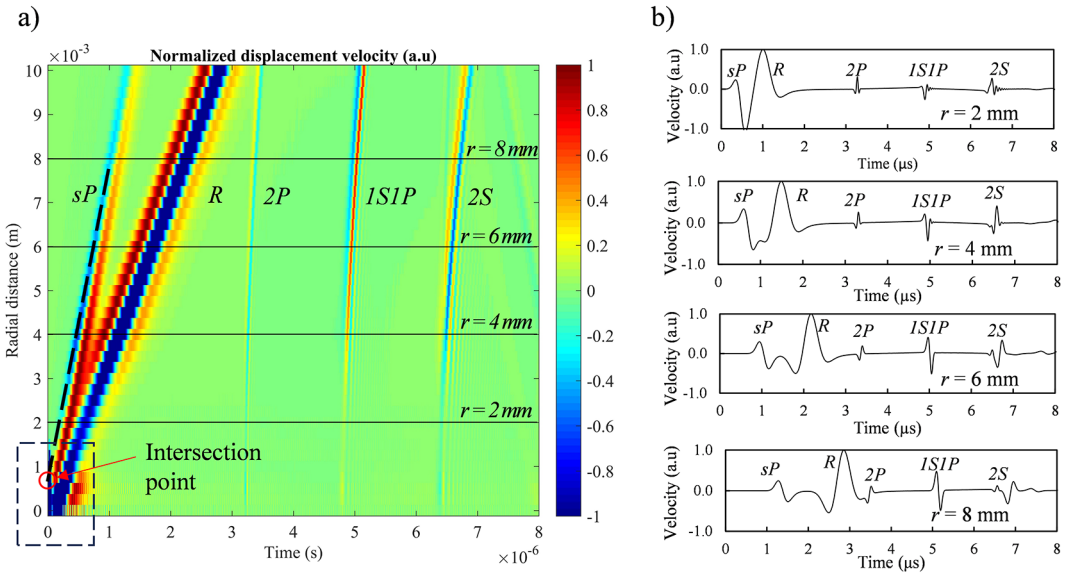

Figure 3. (a) Time-position image of the normalized displacement velocity obtained from simulation; (b) simulated waveforms extracted from time-position image

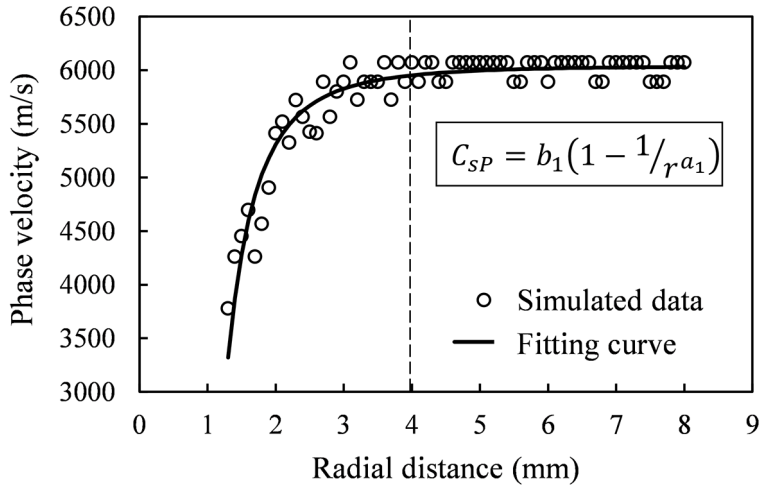

Figure 4. Phase velocity of skimming longitudinal wave depending on the radial distance

different wave modes in the time domain do not overlap when the radial distance of the inspection point varies between 4 and 8 mm. When the radial distance is 2 mm, the tail of the *sP* wave is overlapped by the beginning of the *R* wave. In addition, the order of signal appearance is *sP*, *R*, *2P*, *1S1P*, and *2S*, respectively, simplifying signal detection in the time domain without the need for complex identification methods such as frequency analysis.

In this study, we utilized numerical simulation to determine the characteristics of the propagation velocity of laser-generated ultrasound waves. The velocity of the *sP* (C_{sP}) was proved to depend on the Poisson's ratio [23] or the frequency of its signal [24]. Specifically, C_{sP} was found to be less than C_P when the Poisson's ratio is greater than 0.26 [23, 25], and conversely, when the Poisson ratio is less than 0.26, C_{sP} was assumed to be equal to C_P [24, 25]. The above studies also do not propose a specific formula to calculate C_{sP}. Instead, a straightforward method for determining the phase velocity of *sP* involves comparing the signals of these waves at two distinct locations. Our study evaluated the relationship between the phase velocity of the *sP* wave and the radial distance of the inspection point located on the surface, as depicted in Figure 1d. The data from the time-position image in Figure 3a was utilized to extract the waveform at various inspection points. By comparing the time difference between the

Table 1. Summary of least square fitting results for phase velocity of skimming longitudinal wave depending on the radial distance

Coefficients (with 95% confidence bounds)		Goodness of fit			
a_1	b_1	SSE	R^2	$R^2(adj)$	RMSD
3.04±0.24	6041.45±62.91	1.76×10^{-6}	0.8996	0.8034	55.65

peaks of two successive *sP* signals with a spacing of 0.1 mm, the phase velocity was determined. Figure 4 describes the results of phase velocity of *sP* wave obtained at various inspection points depending on the radial distance. Table 1 provides a summary of the results of fitting discrete data with the formula shown in Figure 4. The coefficient of determination $R^2 = 0.8996$ closes to 1 and the root mean square deviation (*RMSD*) of 55.65 shows the good fitting results. The fitting curve demonstrated that when the inspection point is close to the source, the velocity of *sP* is lower compared to distances far from the source. This is explained by the tail of *sP* signal being overlapped by the beginning of *R* signal, resulting in a change in the slope of the rising part of the *sP* signal. As this distance gradually increases, specifically beyond 4 mm, the *sP* signal begins to separate from the *R* signal, and the velocity of the *sP* can be considered constant. On the other hand, the phase velocities of the *P* (C_P) and *S* (C_S) were theoretically calculated from the elastic modulus, Poisson's ratio, and density of the material [2]. Therefore, the velocities of these two waves were considered constants depending on the properties of the material. Hence, the C_{sP}/C_P ratio can be considered constant at the inspection point far from the source. This conclusion has significant implications for combining *sP* waves and *P* waves to extract crucial material properties.

Dung [17] used an experimental method to determine C_{sP} and C_P on reference specimens cut from the same ingot made of AA 6061, then the C_{sP}/C_P ratio was estimated as 0.95 ± 0.01. This method reveals a major drawback when it cannot be applied directly to specific specimens. In this study, the numerical method was utilized to deduce the constant ratio of C_{sP}/C_P at the radial distance exceeding 4 mm. A total of 30 numerical models were used to derive the C_{sP}/C_P ratio for AA 6061 material, with the elastic modulus varying between 69 GPa and 72 GPa in 1 GPa increments, Poisson's ratio varying from 0.30 to 0.35 with an increment of 0.01, while the density and thermal properties remained unchanged. Figure 5 shows a linear relationship between C_{sP}/C_P ratio and C_{sP}. Table 2 summarizes the results of the least square fitting, demonstrating that the prediction model has a good linear fit with R^2 of 0.8725 and the *RMSD* of 0.002. In conclusion, since the *sP* wave propagates along the surface of the object and is not influenced by reflected waves from the back surface, as illustrated in Figure 3a, the prediction model based on the simulation of a plane plate can be effectively applied to a sloped plate. This approach allows for the determination

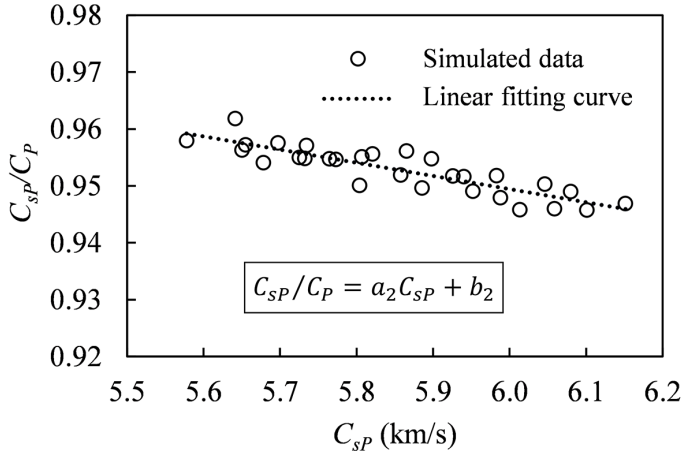

Figure 5. Prediction model to determine the ratio between velocities of skimming longitudinal wave and bulk longitudinal wave for AA 6061

Table 2. Summary of least square fitting results of prediction mode

Coefficients (with 95% confidence bounds)		Goodness of fit			
a_2	b_2	SSE	R^2	$R^2(adj)$	RMSD
-0.0232±0.0022	1.0885±0.0093	0.106×10^{-3}	0.8725	0.8544	0.002

of the C_{sP}/C_P ratio through the C_{sP} obtained by scanning the generating laser directly on the surface of the sloping specimen whose thickness is to be determined.

METHOD FOR SIMULTANEOUS MEASUREMENT

Principle of method

In this study, a new method is proposed to simultaneously determine the thickness, ultrasonic wave velocity, considering the slope of the slope plate. The proposed method was based on determining the arrival time of different signals appearing on a waveform when separating the generating laser (*GL*) and receiving laser (*RL*), including the *2S*, *2P*, *1S1P*, and *sP* signals. Figure 6 illustrates the propagation path of multiple ultrasonic waves when the *RL* is perpendicular to the front plane of the slope plate and the *GL* is on the left side. L_c is the separated distance between the center of two laser spots. H_1 is the thickness at the location of the *RL* spot, and H_2 is the thickness at the location of the *GL* spot. The back surface of the specimen has a slope of $a = \tan\gamma$, where a positive value indicates that H_2 is greater than H_1, and vice versa. In Figure 6a, θ is the incident and reflected angles of the *2S* wave and *2P* wave. In Figure 6b, α and β are the incident angle and the reflected angle of *1S1P* wave, respectively. Considering the *GL* spot is the point source generated ultrasonic wave, the travel distance of multiple wave modes can be calculated using the geometrical relationship.

The arrival time of *2S* and *2P* waves propagated in the medium corresponding to their propagation paths described in Fig. 6a considering the slope of reflected surface, namely, t_{2P} and t_{2S} are expressed in the following Equations:

$$t_{2P} = \frac{\sqrt{L_c^2 + (2H_1 + aL_c)^2}}{C_P}\frac{1}{\sqrt{1+a^2}} \tag{8}$$

$$t_{2S} = \frac{\sqrt{L_c^2 + (2H_1 + aL_c)^2}}{C_S}\frac{1}{\sqrt{1+a^2}} \tag{9}$$

where: C_S – velocity of *S* wave, C_P – velocity of *P* wave.

The ratio between C_S/C_P can be estimated from Equation 8 and Equation 9 as follows:

$$\frac{C_S}{C_P} = \frac{t_{2P}}{t_{2S}} \tag{10}$$

The arrival time of *1S1P* wave corresponding to its propagation paths described in Figure 6b considering the slope of reflected surface, namely, t_{1S1P} is expressed in the following Equations

$$t_{1S1P} = \left(\frac{H_1 + aL_c}{C_S\cos\alpha} + \frac{H_1}{C_P\cos\beta}\right)\frac{1}{\sqrt{1+a^2}} \tag{11}$$

In the case of conversion mode, the ultrasonic wave from the angle propagation is reflected at

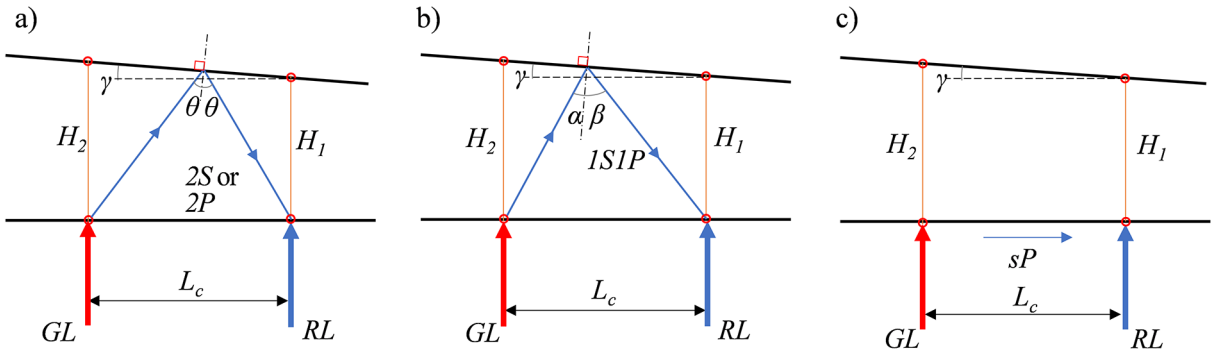

Figure 6. Propagation wave paths to determine the travel distance of multiple wave modes: (a) reflected waves, (b) mode-converted waves, (c) skimming longitudinal wave

the interface between material and air in accordance with Snell's law:

$$\frac{\sin\alpha}{\sin\beta} = \frac{C_S}{C_P} \tag{12}$$

$$L_c = (H_1 + aL_c)\tan\alpha + H_1 \tan\beta \tag{13}$$

The arrival time of *sP* wave propagated along the front surface corresponding to its propagation paths described in Fig. 6c, namely, t_{sP} is expressed in the following Equations:

$$t_{sP} = \frac{1}{C_{sP}} L_c = \left(\frac{C_{sP}}{C_P}\right)^{-1} \frac{L_c}{C_P} \tag{14}$$

where: C_{sP} – velocity of *sP* wave.

As discussed in the simulated result, multiple wave modes can be acquired separately at a properly separated distance between the *GL* and *RL*. Figure 7 presents the typical experimental waveform obtained on the slope plate where the signals *sP*, *2P*, *1S1P,* and *2S* have appeared sequentially. Therefore, the arrival time of each signal was determined using the difference in time between the onset of the photodetector signal and the onset of the signal on the time domain [17].

An important note drawn from the simulated results in Figure 3a shows that the *sP* wave is considered to originate from the edge of the disk source excited by the Gaussian laser. Therefore, the influence of the disk source radius, R_0, needs to be considered in the calculations because the above Equations established for the point source may lead to errors. Figure 8 schematically illustrates the influence of the ultrasonic disk source on calculating the travel distance of multiple wave modes where the ultrasonic disk source is considered as the combination of multiple point sources. To evaluate the influence of the radius of the ultrasonic disk source on the calculations, three cases were implemented to estimate the travel distances, thereby validating the proposed method.

- Case 1 – R_0 is considered for t_{sP}, but not for t_{2P}, t_{2S}, and t_{1S1P};
- Case 2 – R_0 is considered for t_{sP}, t_{2P}, t_{2S}, and t_{1S1P};
- Case 3 – R_0 is not considered for t_{sP}, t_{2P}, t_{2S}, and t_{1S1P}.

Finally, if the C_{sP}/C_P ratio is considered a known parameter, hence the system of six Equations from Equation 9 to Equation 14 can be solved using the Generalized reduction gradient nonlinear solving method, which gives the six solutions H_1, a, C_P, C_S, α, and β (reflected angle of mode-converted longitudinal wave). The method to determine the C_{sP}/C_P ratio and R_0 in the experiment will be described in the next Section.

Determine C_{sP}/C_P and R_0 by scanning the generating laser

To address the limitation of relying on a reference specimen for determining the C_{sP}/C_P ratio [17], the proposed method utilizes the prediction model depicted in Figure. 5. This model enables predicting this ratio using the C_{sP} obtained through scanning *GL* on the surface of the specimen before conducting the collection of data for simultaneous measurement. Equation 15 was established to describe the linear relationship between propagation distance and the arrival time of *sP* signal:

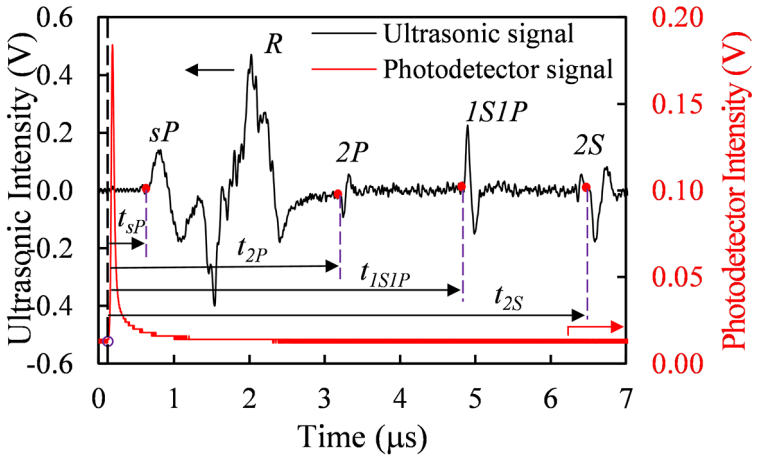

Figure 7. Arrival time determined on typical waveform based on the onset detection

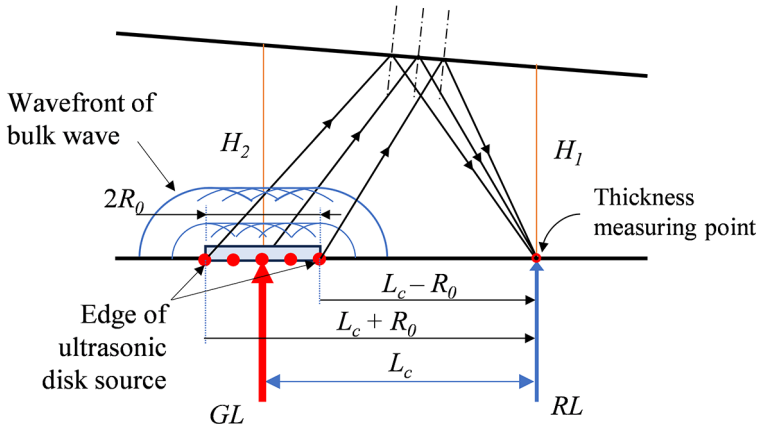

Figure 8. Diagram illustrating the influence of the ultrasonic disk source on the calculation of the travel distance for multiple wave modes

$$L_c = C_{sP} t_{sP} + R_0 \tag{15}$$

where: C_{sP} – velocity of *sP* wave in km/s, R_0 – radius of ultrasonic disk source in mm as depicted in Figure 8.

The arrival time of the *sP* signal, t_{sP}, which corresponds to the separated distance, L_c, is extracted from scanning results. The least square technique is utilized to fit the sets (t_{sP}, L_c) to Equation 15. Therefore, the slope and intercept of linear fitting curve represent the values of C_{sP} and R_0. As discussed above, at the separated distance of *RL* far from the *GL*, the phase velocity of the *sP* and C_{sP}/C_P ratio are assumed to be constant. Therefore, the fitting technique was carried out with a separated distance exceeding 4 mm.

SPECIMENS AND EXPERIMENTS

Specimens

Five specimens cut from an ingot made by Aluminum alloy 6061-T651 (according to JIS H 4000 standard) were prepared. Table 3 presents the dimension of five specimens with H_{max} almost constant of approximately 10 mm, while H_{min} varies is consistent with the change of slope angle. Here, H_{min} and H_{max} represent the minimum and maximum thickness of the specimen, respectively, measured using a micrometer (Mitutoyo Corp., Japan) with a precision of 0.01 mm. The specimen width, L_S, was measured using calipers (Mitutoyo Corp., Japan) with a precision of 0.02 mm. The actual slope in percentage, %*a*, was calculated according to the following formula:

$$\%a = \frac{H_{max} - H_{min}}{L_S} 100\% \tag{16}$$

To validate the wave velocities measured by the proposed method, the elastic wave velocities were determined by theoretical calculations using Equation 17 and Equation 18 [2].

$$C_P = \sqrt{\frac{E(1-\nu)}{\rho(1+\nu)(1-2\nu)}} \tag{17}$$

$$C_S = \sqrt{\frac{E}{2\rho(1+\nu)}} \tag{18}$$

Table 3. Dimension of specimens for laser ultrasonic testing

Sample	L_s (mm)	H_{max} (mm)	H_{min} (mm)	*a* (%)	Cross-section of specimen
1	100.10±0.02	10.12±0.01	10.11±0.01	0.00±0.01	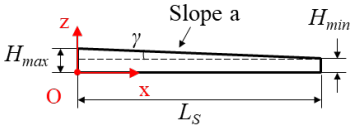
2	100.10±0.02	10.11±0.01	9.60±0.01	0.51±0.01	
3	100.10±0.02	10.05±0.01	9.14±0.01	0.91±0.01	
4	100.20±0.02	10.04±0.01	8.59±0.01	1.45±0.01	
5	100.20±0.02	10.07±0.01	8.11±0.01	1.96±0.01	

where: E – Elastic modulus, v – Poisson's ratio, ρ – density.

Elastic modulus and Poisson's ratio were determined via compression testing using a universal testing machine (UH-X/FX series, Shimadzu Corp., Japan) on specimens measuring 10 × 10 × 18 mm, cut from the same ingot. In addition, the density was measured using Archimedes' density measurement method. Therefore, the calculated values of C_P and C_S were 6263 ± 80 m/s and 3155 ± 40 m/s, respectively.

Experiments

In Figure 9a, the experimental setup incorporates a Q-switched pulsed Nd: YAG laser (the Ultra 50 Laser system from Quantel laser by Lumibird Inc., USA). This pulsed laser has a wavelength of 1064 nm with a repetition rate of 20 Hz, providing a maximum laser energy output of 50 mJ. For detecting surface displacement induced by ultrasonic waves, an IOS AIR-1550-TWM laser ultrasound receiver (Intelligent Optical Systems Inc., Torrance, California, USA) is utilized. This receiver employs the two-wave mixing method within an optical refractive crystal, offering a bandwidth of 125 MHz and a maximum power of 2 W. The receiver system comprises a continuous laser operating at a wavelength of 1550 nm, along with a demodulator, a splitter module dividing the laser output into probe and reference beams, and a measured head. The signal was processed through a differential circuit before being captured by the oscilloscope, resulting in a signal that is proportional to the displacement velocity of the inspection point normal to the surface.

To precisely determine the initial time of the ultrasonic signal, a photodetector, specifically the EOT ET-2030 (Coherent Corp. USA), was employed to measure the intensity of the scattered laser from the front surface of the material. Signal conversion to digital format was carried out using a high-resolution oscilloscope, the GDS 2202A (Good Will Instrument Corp., Ltd., Taiwan), with a sampling rate of 2 ns at a time scale of 10 µs. Each signal was averaged 256 times to enhance its quality by reducing noise. A rotating mirror system (Newport Corp. Japan) was employed for adjusting the generating laser spot on the surface, consisting of a picomotor mirror mount controlled by a picomotor controller kit via software installed on a computer.

Before testing, seven thickness measuring points were specified along the horizontal line on each specimen, as depicted in Figure 9b. The initial point for thickness measurement was set with a horizontal distance of 30 mm from the edge of the specimen to avoid the influence of the guide wave signal reflecting from this edge, with subsequent thickness measuring points spaced at intervals of 10 mm. The specimen was carefully fixed on the manual translation stages, ensuring surface of the specimens is perpendicular to the receiving laser beam. The thickness measured by the proposed method represents the thickness of the specimen at the location of the receiving laser spot.

Initially, the experiment was performed by scanning the generating laser to determine the skimming longitudinal wave velocity and the radius of the ultrasonic disk source. By rotating the mirror, the picomotor control kit allows the generating laser spot to be incrementally shifted by 0.2 mm. The separated distance was adjusted

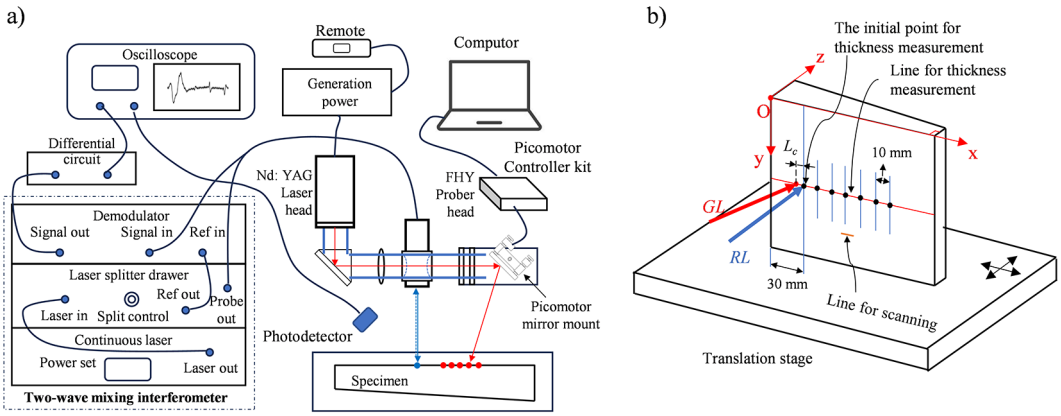

Figure 9. (a) Schematic diagram of the experimental setup, (b) diagram illustrating the scanning line and thickness measuring points on the specimen

from 0 mm to 10 mm. Subsequently, select the appropriate separated distance so that the signals of the *sP*, *R*, *2P*, *1S1P*, and *2S* waves displayed on the oscilloscope do not overlap as the typical waveform depicted in Figure 7. Then, shift the specimen to the position where the *RL* focused on the thickness measuring point using the translation stage without altering the laser setup. Thirty measurements for each thickness measuring point were carried out to collect the waveform for data processing. Using the solving tool integrated in Microsoft Excel 365, the system of Equations was solved. The uncertainties of input quantities, which include t_{sP}, t_{1S1P}, t_{2S}, L_c, and ratio C_{sP}/C_P as well as the combined standard uncertainties of output quantities, comprising H_1, C_P, C_S, and $\%a$ were determined in accordance with the standard JCGM 100: 2008 [26].

overlapped by the *R* signal. This shows the effectiveness of the proposed numerical simulation for guided waves. In addition, this consistency supports the condition for fitting the *sP* curve from the experimental data in the range of scanning distance from 4 to 8 mm to deduce the constant value of C_{sP}, as explained by the simulated results.

The discrete points (t_{sP}, L_c) were then fitted with Equation 15 as depicted in Figure 11. Table 4 summaries the least square fitting results that show the good linear fit with the high R^2 of 0.9975 and low *RMSD* of 0.02, yielding a slope of the linear fitting line as the C_{sP} of 5.99 ± 0.05 km/s and the intercept as R_0 of 0.90 ± 0.02 mm. Using the prediction model mentioned in Figure 5 and Table 2, the C_{sP}/C_P ratio, determined from the C_{sP} measured by the scanning technique, was rounded to three decimal places as 0.950 ± 0.015.

EXPERIMENTAL RESULTS AND DISCUSSION

Calculation of C_{sP}/C_P and R_0

Figure 10a displays the normalized intensity of the ultrasonic signal obtained from scanning the generating laser along the surface, presented as a time-position image. The *sP* wave shows an obvious linear relationship in the range of 4 to 8 mm aligned with the simulated result shown in Figure 3a. Extracting waveforms at two separated distances of 4 mm and 8 mm, Figure 10b shows that the experimental waveforms displaying the *sP* and *R* signals are consistent with the simulation results, clearly indicating that the *sP* signal is not

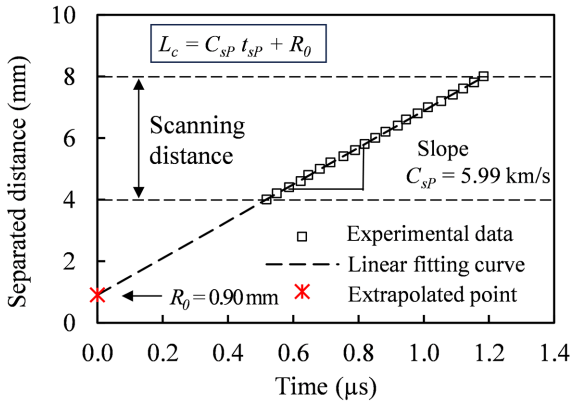

Figure 11. Determination of the skimming longitudinal wave velocity (C_{sP}) and radius of the ultrasonic disk source (R_0) using the least square technique

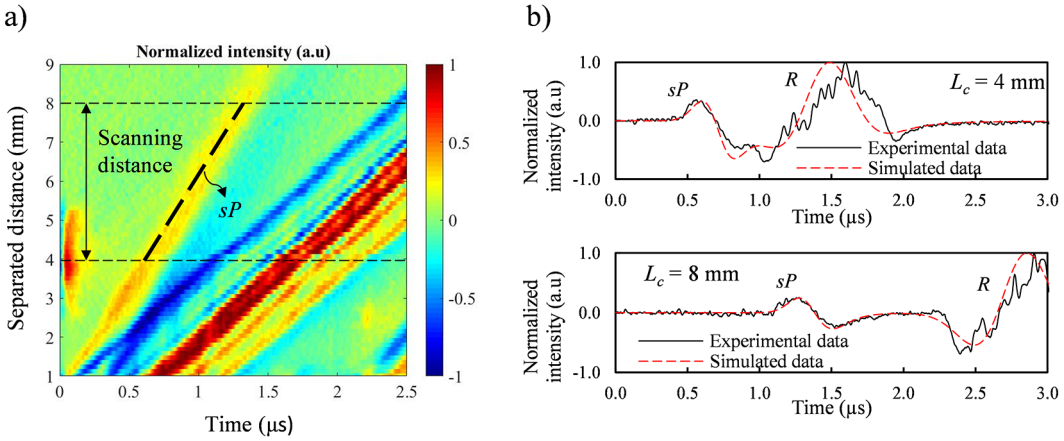

Figure 10. Scanning results: (a) time-position image obtained from the experiment, (b) extracting the waveform at separated distances of 4 and 8 mm

Table 4. Summary of least square fitting results to determine C_{sP} and R_0

Sample	L_S (mm)	H_{max} (mm)	H_{min} (mm)	a (%)	Cross-section of specimen
1	100.10±0.02	10.12±0.01	10.11±0.01	0.00±0.01	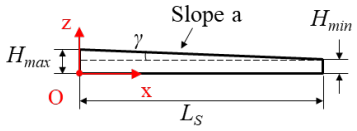
2	100.10±0.02	10.11±0.01	9.60±0.01	0.51±0.01	
3	100.10±0.02	10.05±0.01	9.14±0.01	0.91±0.01	
4	100.20±0.02	10.04±0.01	8.59±0.01	1.45±0.01	
5	100.20±0.02	10.07±0.01	8.11±0.01	1.96±0.01	

The uncertainty of this ratio considered the uncertainty of the prediction model and the C_{sP} obtained by fitting the scanning data. This ratio and the radius of the ultrasonic disk source were used in the proposed method to calculate the thickness, slope and wave velocities of the slope plates.

Thickness, slope and wave velocities measurement

After determining the ratio C_{sP}/C_P and R_0, the proposed method allows calculating the slope, thickness and ultrasonic wave velocity simultaneously by solving the system of Equations. To evaluate the feasibility of the proposed method, four specimens with slopes of 0.51%, 0.91%, 1.45%, and 1.91% were employed, respectively. Measurements were carried out at seven points located along the horizontal line on each specimen. The results of thickness and slope at the receiving laser spot are depicted in Figure 12 and Figure 13, respectively. It is clear to see in Figure 12 that the thickness calculation results in Case 1 and Case 2 agree well with the actual thickness for all specimens, while Case 3 shows large errors compared with the actual thickness. Figure 13 shows the slope measurement results of the proposed method, only Case 1 consistently aligns with the actual slope for all specimens. The positive slope value aligns with the calculation assumptions. These findings underscore the importance of considering the influence of the radius of the ultrasonic source for accurately determining the travel time of the *sP* wave. Conversely, such consideration is unnecessary when calculating the travel distance

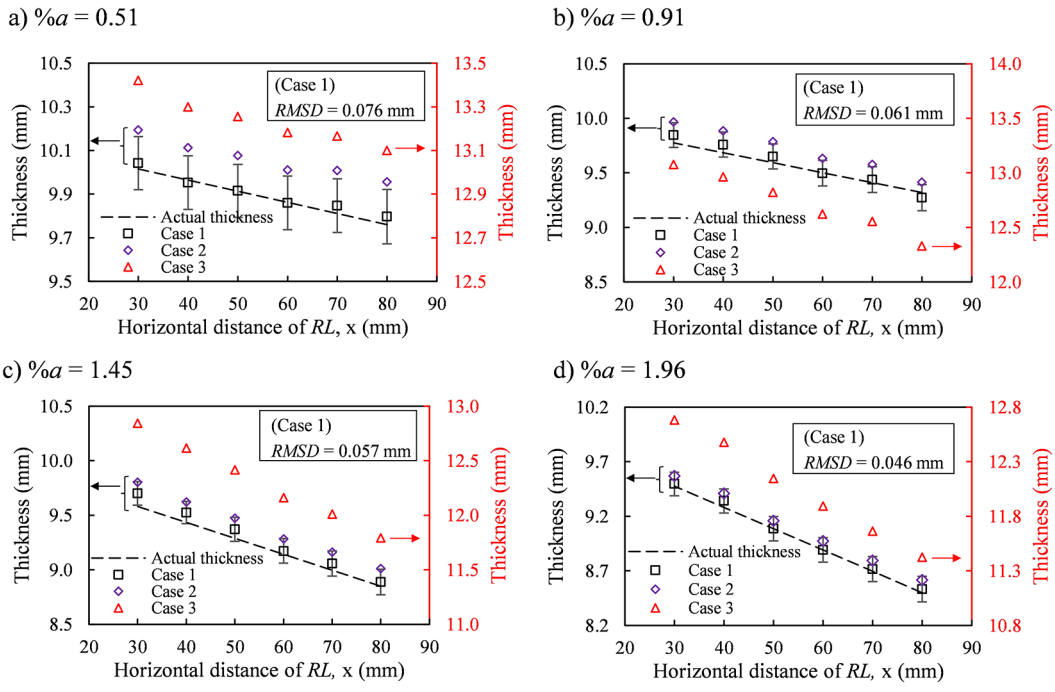

Figure 12. Thickness measurement for plates with the slope: (a) %a = 0.51; (b) %a = 0.91; (c) %a = 1.45; (d) %a = 1.96

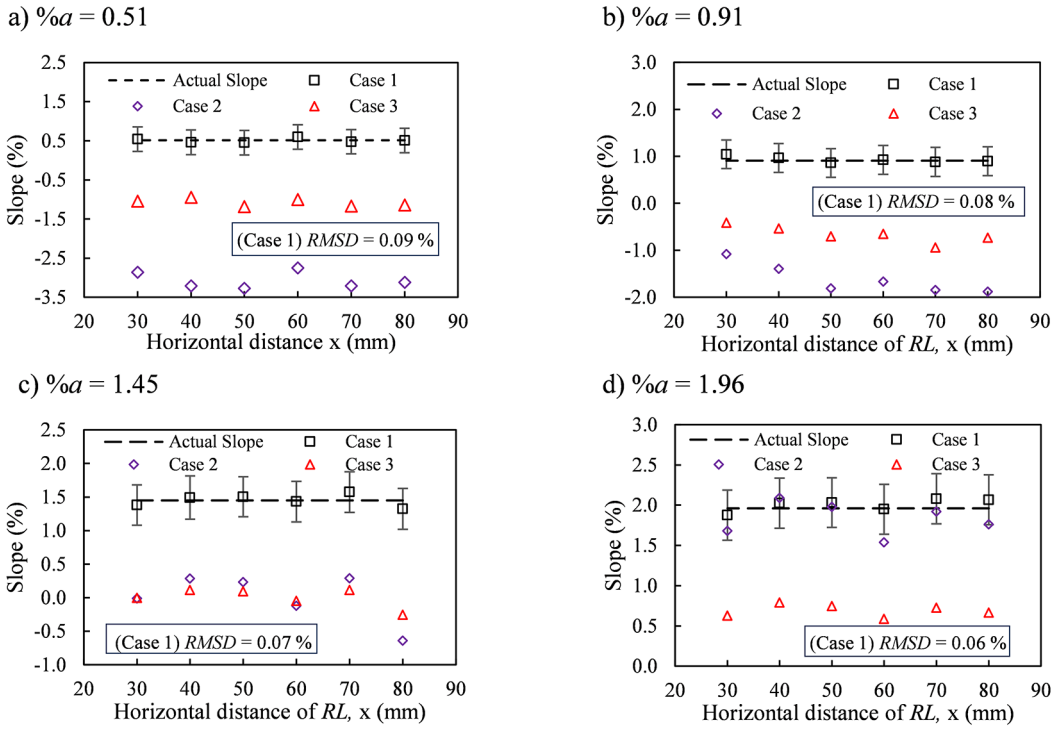

Figure 13. Slope measurement for plates with the slope: (a) %a = 0.51; (b) %a = 0.91; (c) %a = 1.45; (d) %a = 1.96

of bulk waves in the proposed method. This can be explained because the signal of the reflected waves obtained on the waveform is the interference of signals originating from point sources located on the disk plane source. Due to the symmetrical nature of the disk source, bulk waves should be considered starting from the center of the disk source. Therefore, the next evaluations are performed on the proposed method using Case 1. Then, *RMSD* between the actual parameters and calculated results was determined to evaluate the accuracy of the proposed method. *RMSD* is depicted in Figure 12 and Figure 13 for each specimen. The maximum *RMSD* of 0.076 mm for thickness measurement and 0.09% for slope measurement demonstrate the high accuracy of the proposed method, validating the effectiveness of the proposed method. Figure 12 and Figure 13 also show the combined standard uncertainty obtained at each measured point. The proposed method also demonstrates high precision, with an average uncertainty of thickness measurement of around 0.120 mm and slope measurement of around 0.40%.

Figure 14 proves the ability of the proposed method using Case 1 to determine the thickness and slope of the 10-mm-plane plate. The results were then compared with the technique mentioned by Dung [17] which just applies to plane plates. The comparison shows that the proposed method can be completely applied to the plane plate because these two methods show the same thickness and slope results as well as the uncertainty. The *RMSD* of the proposed method when determining the thickness and slope of the plane plate with an actual thickness of approximately 10 mm is about 0.100 mm and 0.10%, respectively. In addition, the proposed method shows the uncertainty for thickness and slope measurement of around 0.140 mm and 0.40% in this case.

Figure 15a and Figure 15b present the distribution of *RMSD* of thickness and slope measurement depending on the change of the slope of the specimens determined using case 1. The maximum *RMSD* for thickness and slope measurements is observed when applying the proposed method to plane plate. The finding is that the *RMSD* of thickness measurement tend to decrease as the slope angle increases. This can be explained by considering the bulk wave to originate from a point source located at the center of the laser spot. Figure 15c illustrates discrepancies between the actual wavefront and the assumed wavefront used in the calculation. Consequently, when the slope changes, the error in calculating the travel distance changes, leading to a variation

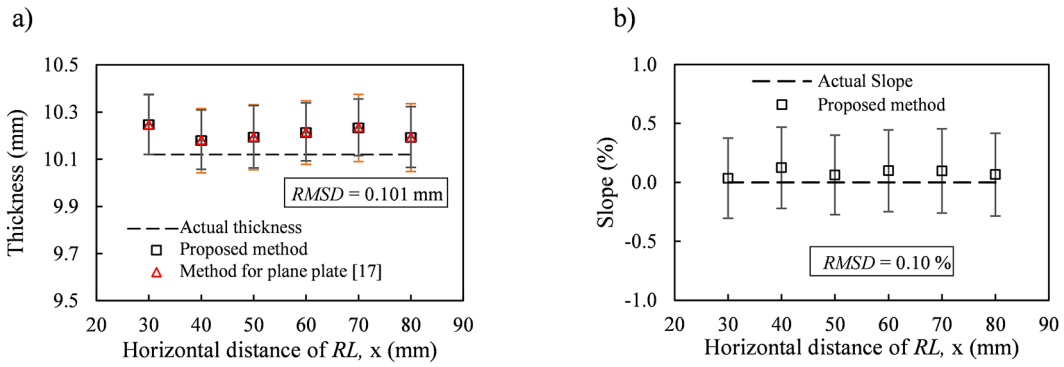

Figure 14. Applying the proposed method for plane plate: (a) thickness measurement, (b) slope measurement

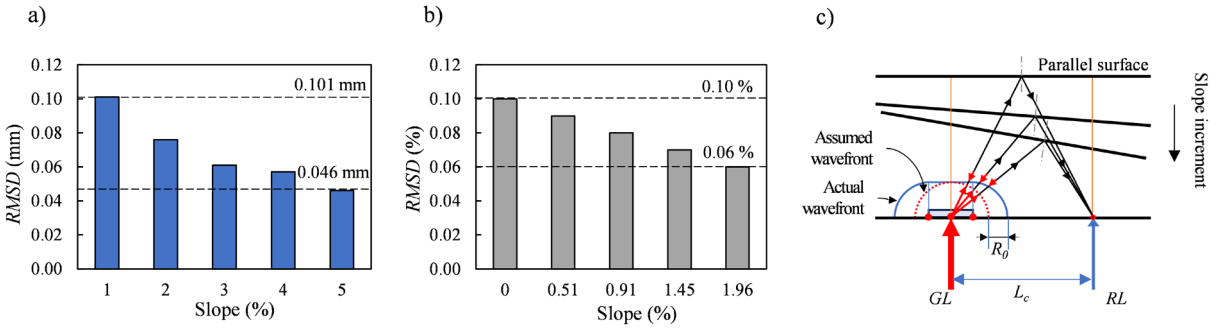

Figure 15. The *RMSD* of thickness and slope measurement depend on the slope of the specimen using Case 1: (a) thickness measurement, (b) slope measurement, (c) diagram to explain the error on travel distance that arises when slope increases

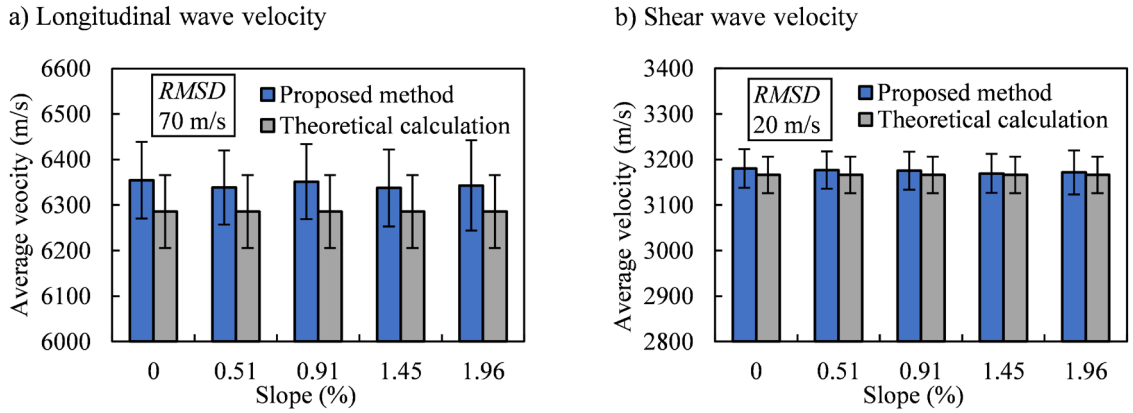

Figure 16. Comparison of velocity measurements to theoretical calculations

in thickness error. However, this variation can be considered negligible due to the acceptable range of *RMSD*, which remains between 0.046 mm and 0.101 mm. Accordingly, the maximum *RMSD* of slope measurement can be accepted at around 0.10%. Figure 16 compares the results of C_P and C_S with the theoretical calculation deduced from the elastic constant and density. *RMSD* of wave velocity measurements is 70 m/s for longitudinal wave and 20 m/s for shear wave, respectively. The greater error of C_P is explained by the fact that C_P was calculated by predicting the C_{sP}/C_P ratio through simulation. Compared with the method mentioned by Chen [14], which has a velocity measurement error of approximately 70 m/s when calculating simultaneously with thickness, the proposed method shows similar performance. The combined standard uncertainties of the wave velocity measurements were calculated and shown in Figure 16. The uncertainties of the

longitudinal wave and shear wave velocities are approximately 90 m/s and 40 m/s, respectively, and do not vary significantly with changes in slope. This result shows that this measurement has precision equivalent to theoretical calculations.

CONCLUSIONS

In this work, a reliable method for calculating the thickness and slope without the knowledge of bulk wave velocity for slope plates is introduced and evaluated using the laser ultrasonic technique within the thermoelastic regime. The combination of multiple wave modes, including the skimming longitudinal wave, reflected waves, and mode-converted waves, is used to extract the desired parameters by solving the system of Equations determining the arrival time of the signals obtained on a waveform. The feasibility of the method was evaluated by experiments performed on five specimens made of AA 6061 with different slopes of 0 %, 0.51%, 0.91%, 1.45%, and 1.96%, respectively. Some main results obtained are as follows:

The velocity of the skimming longitudinal wave is approximately 95% of the bulk longitudinal wave velocity for aluminum material. To enhance the accuracy of calculations when combining longitudinal and bulk waves to deduce the desired parameters, the prediction model established using numerical methods allows this ratio to be estimated by using the skimming longitudinal wave velocity obtained from scanning the surface of the specimen for thickness testing.

The ultrasonic source generated by the unfocused laser is considered as the plane disk source in the calculation. Therefore, the skimming longitudinal wave is proved to propagate from the edge of the disk source. In contrast, the bulk wave can be considered to originate from the center of the disk source.

The proposed method demonstrates high accuracy with the maximum root mean square deviation compared to actual thickness and slope being around 0.100 mm and 0.10% when varying the slope in the range of 0 to 2%.

The root mean square deviation of velocity measurements compared to theoretical calculations is determined as 70 m/s for the longitudinal wave and 20 m/s for the shear wave, respectively. Future research will involve testing the proposed method on a variety of materials to assess its practical feasibility.

Acknowledgements

The authors are grateful for the financial support provided by the Ministry of Education, Science, Sports, and Culture of the Government of Japan (MEXT).

REFERENCES

1. Hutchins D.A. Ultrasonic generation by pulsed lasers. (Physical Acoustics). San Diego (CA): Academic Press. 1988; 18: 21–123. https://doi.org/10.1016/B978-0-12-477918- 1.50008-4
2. Scruby C.B., Drain L.E. Laser ultrasonic techniques and applications (1st ed.). New York (NY): CRC Press. 1990. https://doi.org/10.1201/9780203749098
3. Monchalin J., Héon R., Ing R.K., Cand A., Lord M., Bussiere J.F., Bouchard P., Aussel J.D., Bernier R., Boudreault A., Padioleau C. Laser-ultrasonics for materials characterization. Nondestructive Testing and Evaluation. 1992; 7(1–6): 119–135. https://doi.org/10.1080/10589759208952993
4. Lévesque D., Kruger S.E., Lamouche G., Kolarik R.V., Jeskey G.V., Choquet M., Monchalin J.P. Thickness and grain size monitoring in seamless tube-making process using laser ultrasonics. NDT & E International, 2006; 39: 622–626. https://doi.org/10.1016/j.ndteint.2006.04.009
5. Fuse N., Kaneshige K., Watanabe H. Development of thickness measurement system for hot steel with laser-ultrasonic wave technology. Materials Transactions. 2014; 55(7): 1011–1016. https://doi.org/10.2320/matertrans.i-m2014811
6. Kruger S.E., Lord M., Monchalin J.P. Laser ultrasonic thickness measurements of very thick walls at high temperatures. AIP Conference Proceedings. 2006; 820: 240–247. https://doi.org/10.1063/1.2184535
7. Li S., Wang H., Guo R., Zhao J., Zheng K., Xu J., Chen S., Jiang Y. Non-destructive testing thickness measurement by laser ultrasound under high temperature. Optik. 2018; 172: 1140–1154. https://doi.org/10.1016/j.ijleo.2018.07.126
8. Rahim M.A., Arai Y., Araki W. Effects of thickness variation due to presence of roller wake on the thickness measurement using laser ultrasonic technique. The International Journal of Advanced Manufacturing Technology. 2024; 132: 339–348. https://doi.org/10.1007/s00170-024-13397-y
9. Hutchins D.A., Dewhurst R., Palmer S. Directivity patterns of laser-generated ultrasound in aluminum. The Journal of the Acoustical Society of America, 1981; 70(5): 1362–1369. https://doi.org/10.1121/1.387126
10. Zhang P., Yin, C., Shen J. Directivity patterns of

laser thermoelastically generated ultrasound in metal with consideration of thermal conductivity. Ultrasonics (Print). 1997; 35(3): 233–240. https://doi.org/10.1016/s0041-624x(96)00106-0

11. Krylov V.V. Directivity patterns of laser-generated sound in solids: Effects of optical and thermal parameters. Ultrasonics. 2016; 69: 279–284. https://doi.org/10.1016/j.ultras.2016.01.011
12. Pei C., Demachi K., Zhu H., Fukuchi T., Koyama K., Uesaka M. Inspection of cracks using laser-induced ultrasound with shadow method: Modeling and validation. Optics and Laser Technology. 2012; 44(4): 860–865. https://doi.org/10.1016/j.optlastec.2011.11.018
13. Falkenström M., Engman M., Lindh-Ulmgren E., Hutchinson B. Laser ultrasonics for process control in the metal industry. Nondestructive Testing and Evaluation. 2011; 26(3–4): 237–252. https://doi.org/10.1080/10589759.2011.573553
14. Chen S., Wang H., Jiang Y., Zheng K., Guo S. Wall thickness measurement and defect detection in ductile iron pipe structures using laser ultrasonic and improved variational mode decomposition. NDT & E International. 2023; 134: 102767. https://doi.org/10.1016/j.ndteint.2022.102767
15. Gao W., Glorieux C., Thoen J. Laser ultrasonic study of Lamb waves: determination of the thickness and velocities of a thin plate. International Journal of Engineering Science. 2003; 41(2): 150–157. https://doi.org/10.1016/s0020-7225(02)00150-7
16. Gao X., Tian Y., Jiao J., et al. Non-destructive measurements of thickness and elastic constants of plate structures based on Lamb waves and particle swarm optimization. Measurement. 2022; 204: 111981. https://doi.org/10.1016/j.measurement. 2022.111981
17. Dung N.T., Arai Y. Simultaneous measurement of thickness and ultrasonic wave velocity using a combination of laser-generated multiple wave modes in the thermoelastic regime. Nondestructive Testing and Evaluation. 2024. Published online. https://doi.org/10.1080/10589759.2024.2370484
18. Xu B., Shen Z., Ni X., Lu J. Numerical simulation of laser-generated ultrasound by the finite element method. Journal of Applied Physics. 2004; 95(4): 2116–2122. https://doi.org/10.1063/1.1637712
19. Liu P., Nazirah AW., Sohn H. Numerical simulation of damage detection using laser-generated ultrasound. Ultrasonics. 2016; 69: 248–258. https://doi.org/10. 1016/j.ultras.2016.03.013
20. Gao J., Cao Y., Lu L., Hu Z., Wang K., Guo F., Yan Y. Study on the interaction between nanosecond laser and 6061 aluminum alloy considering temperature dependence. Journal of Alloys and Compounds. 2022; 892: 162044. https://doi.org/10.1016/j.jallcom.2021.162044
21. Magnes J., Odera D., Hartke J., Fountain M., Florence L., Davis V. Quantitative and Qualitative Study of Gaussian Beam Visualization Techniques. 2008. https://doi.org/10.48550/arXiv.physics/0605102
22. Achenbach J.D. Laser excitation of surface wave motion. Journal of the Mechanics and Physics of Solids. 2003; 51: 1885–1902. https://doi.org/10.1016/j.jmps.2003.09.021
23. Bescond C., Monchalin J., Lévesque D., Gilbert A., Talbot R., Ochiaiet M. Determination of residual stresses using laser-generated surface skimming longitudinal waves. Proceedings Nondestructive Evaluation and Health Monitoring of Aerospace Materials, Composites, and Civil Infrastructure IV. 2005; 5767. https://doi.org/10.1117/12.620374
24. Canfield R.A., Ziaja-Sujdak A., Pitre J.J., O'Donnell M., Ambrozinski L., Pelivanov I. Simultaneous determination of Young's modulus and Poisson's ratio in metals from a single surface using laser-generated Rayleigh and leaky surface acoustic waves. Journal of Applied Physics, 2022; 132(23): 235103. https://doi.org/10.1063/5.0124395
25. Schroder C., Scott W.R. On the complex conjugate roots of the Rayleigh Equation: The leaky surface wave. Journal of the Acoustical Society of America. 2001; 110(6): 2867–2877. https://doi.org/10.1121/1.1419085
26. Joint Committee for Guides in Metrology (JCGM). Evaluation of measurement data - Guide to the expression of uncertainty in measurement. BIPM; 2008. Standard No. JCGM 100:2008.